Supplementary Information for

Giant inverse elastocaloric effect of n-alkanes imbedded in carbon-frame for room temperature thermal management

Molecular dynamics simulations:

The simulations were carried out using LAMMPS [1], employing the Verlet integration algorithm with a time step of 0.5 fs. The latest version of the PCFF potential [2,3] was applied in the model. Long-range van der Waals and Coulomb interactions were computed using the particle-particle particle-mesh (PPPM) method. To prevent non-physical effects in the vicinity of the fracture zone, the cutoff for Lennard-Jones interactions was set to 12.0 Å. Temperature and pressure were regulated using appropriate barostatic and thermostatic techniques. The model systems were initially equilibrated for 3 ns using an isothermal-isobaric (NPT) ensemble, maintaining a constant temperature of 300 K and zero pressure, controlled by the Nosé–Hoover thermostat and barostat. Following this, uniaxial tension or compression tests were conducted along the axis of the carbon nanotubes (CNTs) at a strain rate of 0.0001 ps^{-1} to evaluate their isothermal mechanical properties. The unloading process was performed by reversing the deformation direction. To simulate the electronic-phonon (eC) effect, strain-controlled adiabatic loading was applied along the CNT axis over a period of 12 ns to replicate gradual compression. To accurately capture the substantial volume changes during loading and unloading and to compute the temperature variation (ΔT), an NPT ensemble with a large damping parameter (Tdamp = 100 ns) was used, ensuring the adiabatic nature of the process by preventing heat exchange between the system and the thermostat.

When conducting molecular simulation studies, the measurement process for each adiabatic temperature change follows these steps:

1. First, the simulation system is allowed to reach equilibrium in its final state, a process that lasts for 1 nanosecond (ns).

2. Then, the system is further simulated for an additional 1 ns, during which we collect 100 data points.

3. These data points are used to calculate the average value of the adiabatic temperature change.

4. To ensure the reliability of the results, the process of collecting data points and calculating the average value is repeated 5 times.

Various specific energies in simulations [2][3]:

pe = potential energy
ke = kinetic energy
etotal = total energy (pe + ke)
evdwl = van der Waals pairwise energy (includes etail)
ecoul = Coulombic pairwise energy
elong = long-range k-space energy
etail = van der Waals energy long-range tail correction
epair = pairwise energy (evdwl + ecoul + elong + etail)
ebond = bond energy
eangle = angle energy
edihed = dihedral energy
eimp = improper energy
emol = molecular energy (ebond + eangle + edihed + eimp)
enthalpy = enthalpy (etotal + press*vol)

In this work, due to the small changes in kinetic energy and the work done by external forces on the system compared to the changes in the system's potential energy, it can be approximated that the enthalpy change of the system is equal to the change in the system's potential energy [44]:

$$\Delta H = \Delta E_k + \Delta E_p + p\Delta V \approx \Delta E_p \quad \text{(S1)}$$

$$-T\Delta S = -\Delta E_p + p\Delta V \approx \Delta E_p = \text{epair} + \text{emol} \quad \text{(S2)}$$

The entropy of an alkane system is mainly composed of the entropy due to the relative positional changes between molecules ΔS_1 and the conformational entropy of the molecules themselves ΔS_2:

$$\Delta S_1\ (C_nH_{2n+1}\ \text{molecular pair}) = (\text{evdwl} + \text{ecoul} + \text{elong} + \text{etail})/T \quad \text{(S3)}$$

$$\Delta S_2\ (C_nH_{2n+1}\ \text{molecular conformational}) = (\text{ebond} + \text{eangle} + \text{edihed} + \text{eimp})/T \quad \text{(S4)}$$

Structural stability of 3D carbon-based network：

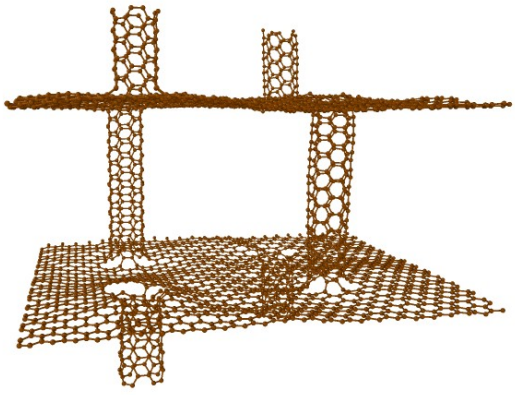

Figure SP1. The ab initio molecular dynamics trajectory.

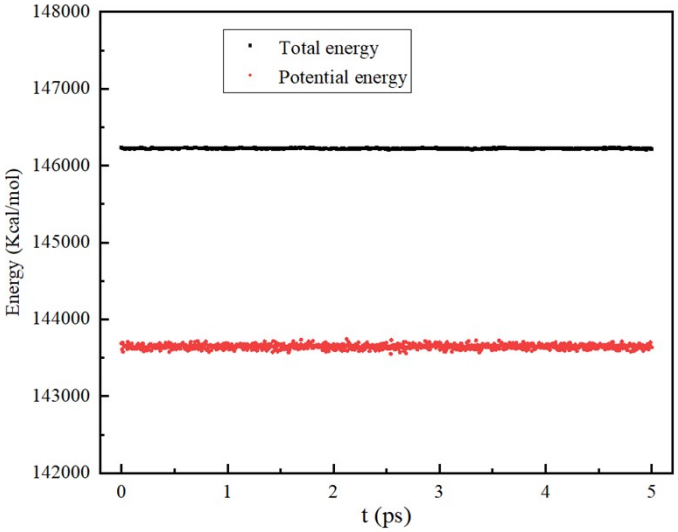

Figure SP2. The relationship between the energy of the 3D carbon nanotube-graphene network structure and time at pressure of 0 GPa and temperature of 300 K.

To demonstrate the stability of the structure used in this work, we conducted ab-initio molecular dynamics simulations (AIMD), of which the results are shown in Fig. SP1 and SP2. It can be seen from the figures that the 3D carbon nanotube-graphene network structure used in this work can stably exist. First-principles-based molecular dynamics is a powerful tool to study the stability of a system. DFT-based molecular dynamics was performed with the Quantum ATK package [40]. Here, the exchange-correlation functional was Perdew-Burke-Ernzerhof (PBE). Dispersion effects have been considered within the Grimme DFT2-D3 van-der-Waals corrections [41]. Molecular dynamics simulations (MD) were performed under NVT canonical ensemble with a target temperature of 300 K by the Nose-Hoover thermostat. The Verlet algorithm was used for integration, and the time-step is 0.5 fs. The simulation time for each MD trajectory is 5 ps, and the thermodynamic quantities of the system are statistically averaged in the last 1 ps.

Validity of MD simulation for the liquid phase:

In this work, we use the long-chain alkane n-heptadecane ($C_{17}H_{36}$) as an example. From experiments, it is known that the melting point of $C_{17}H_{36}$ is 294 K [7], transitioning from solid to liquid, and the density in liquid state is 0.77 g/cm³. Therefore, the $C_{17}H_{36}$ used in this work is in liquid state at 300 K without the need for applying external high pressure, and its density of 0.7 g/cm³ is close to the natural liquid state density. Hence, the use of liquid $C_{17}H_{36}$ alkane in this work is achievable experimentally. Next, we mix the 3D carbon nanotube-graphene network structure with liquid alkanes ($C_{17}H_{36}$). Since alkane is in the liquid state, the molecules randomly distribute within the interlayer structure of graphene. This mixing method has also been reported in other studies [45].

The origin entropy of the elastocaloric effect:

As shown in Fig. SP3, CNT-Gra/C_nH_{2n+1} composites are different from general metal crystals or ionic crystals because alkanes are randomly and disorderly distributed in the carbon framework over long distances. Therefore, when the CNT-Gra/C_nH_{2n+1} composite material is subjected to tension or compression, the volume of the CNT-Gra framework changes, as shown in Fig. SP3 (a) and (b), and the spatial positions and configurations of alkanes change, as shown in Fig. SP3 (c) and (d), just like a rubber.

Furthermore, through the analysis in Fig. SP3 (e), it can be concluded that the entropy change of the composite material is mainly composed of three parts: one is the change in atomic positions leading to a change in pair-entropy, the second is the configurational-entropy related to the change in alkane molecule configurations, and the last one is the sum of other-entropy.

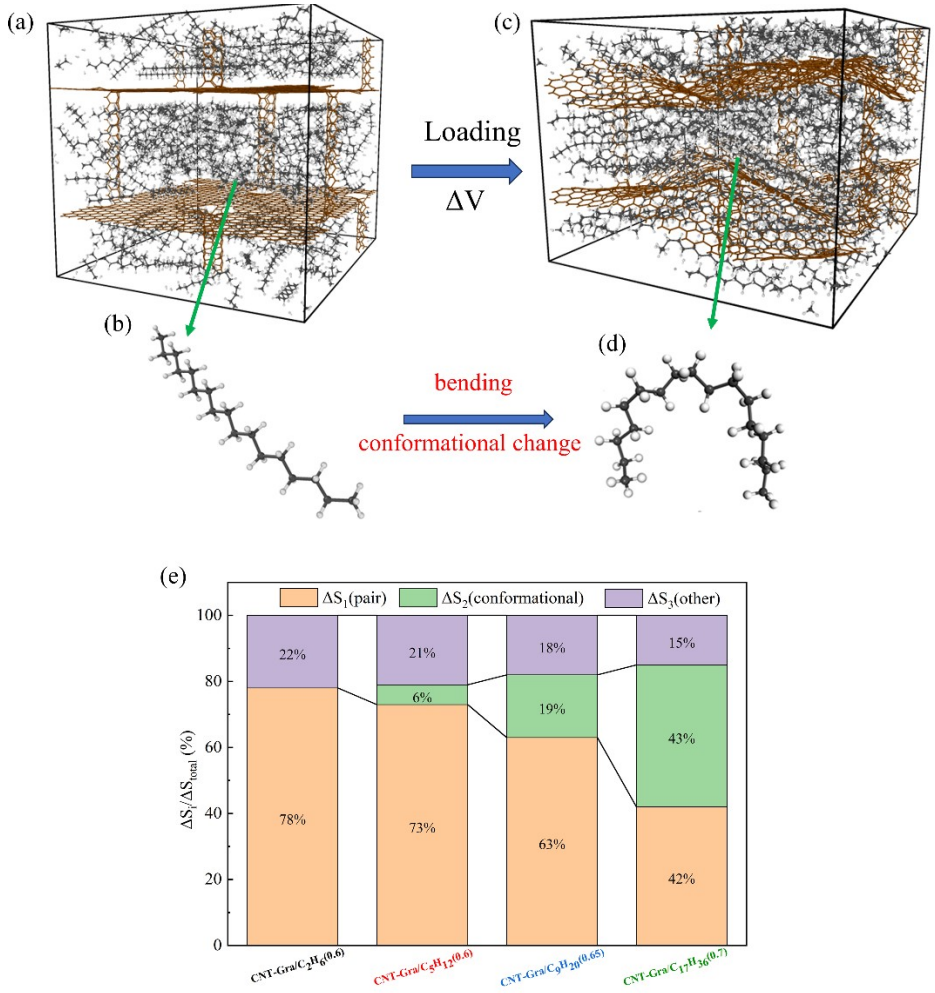

Figure SP3. (a) and (b), the volume change of the composite material under compression. (c) and (d), the change in the configuration of alkane molecules. (f) the proportion of different types of entropy.

Reverse elastocaloric effect:

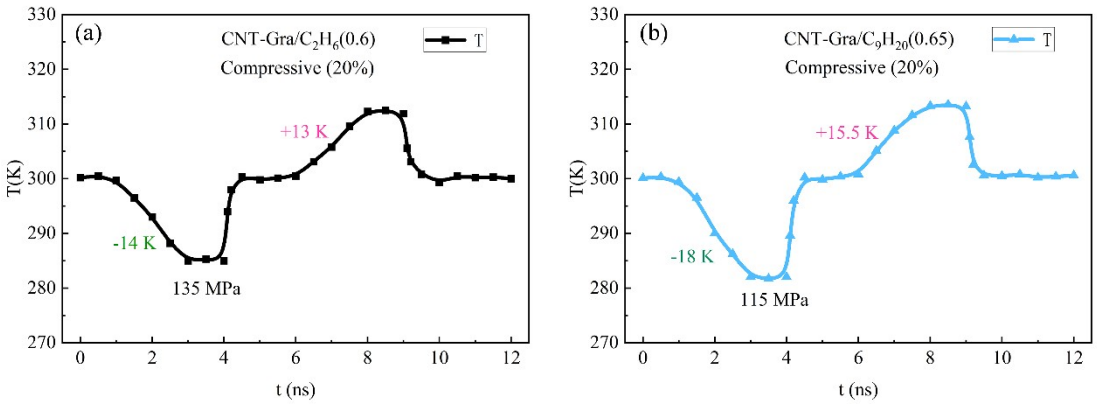

Figure SP4. (a)and (b) The adiabatic temperature ΔT and associated strain as functions of time t at room temperature for various CNT-Gra/C_2H_6 and CNT-Gra/C_9H_{20} composites.

The reverse elastocaloric effects of CNT-Gra/C_nH_{2n+1} composites for n = 2 and 9 are shown in Fig. SP4 (a) and (b).

Stress distribution diagram of CNT-Gra compressed by 20%:

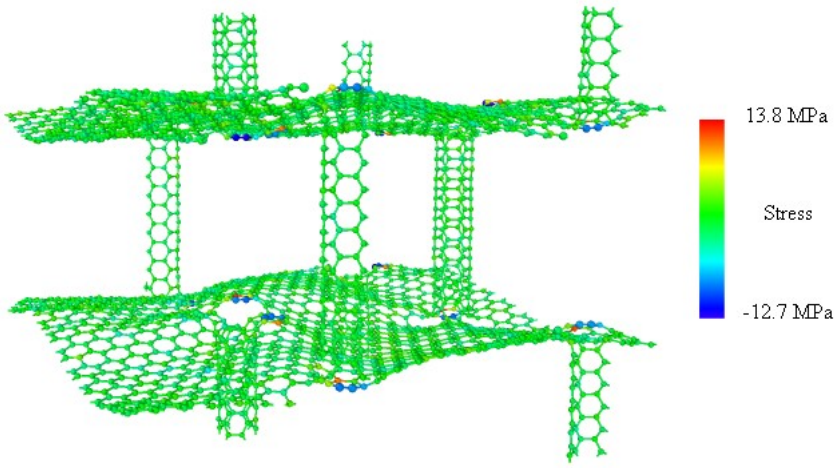

Figure SP5. The stress distribution of the carbon nanotube-graphene framework under a 20% variation along the Z-axis

In our simulation where the composite material was subjected to a 20% strain in the Z-axis direction, we observed the stress distribution of the carbon nanotube-graphene framework (see Fig. SP5). By analyzing this data, we found that the framework can withstand a maximum stress of approximately 13.8 MPa under the experimental conditions. This value is significantly lower than the theoretical fracture strength of graphene, which can reach up to 130 GPa [39].

The trajectory of CNT-Gra/$C_{17}H_{36}$ compressed by 20%:

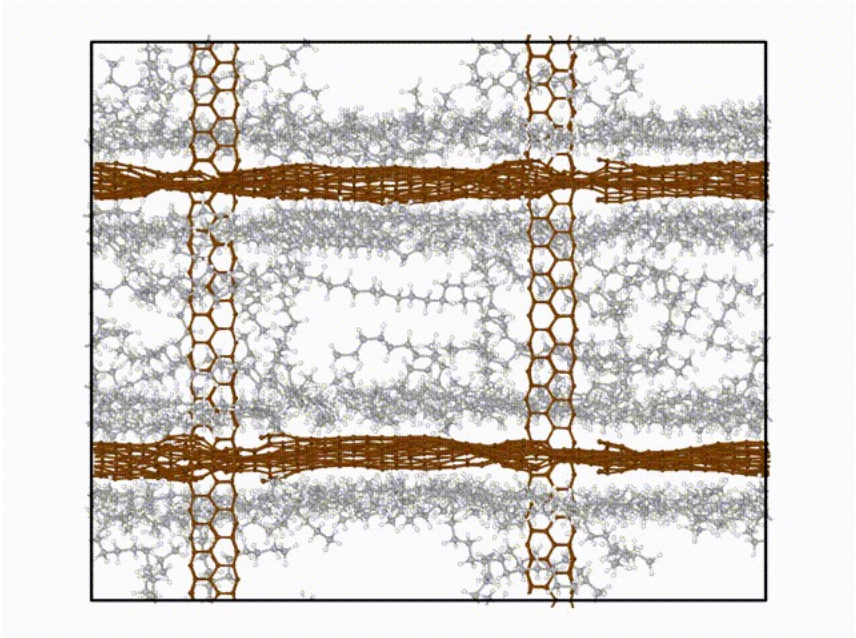

Figure SP6. The molecular dynamics trajectory of CNT-Gra/$C_{17}H_{36}$.

Uniaxial tensile and compressive tests were conducted along the axis of the CNTs at a strain rate of 0.0001 ps^{-1} to characterize their isothermal mechanical properties. The unloading process was executed by reversing the deformation direction. To simulate the eC effect, a strain-controlled adiabatic loading protocol was applied along the CNT axis for a duration of 12 ns, representing a gradual compression process.

CNT-Gra/$C_{17}H_{36}$ (0.7g/cm³) is stretched by 20%:

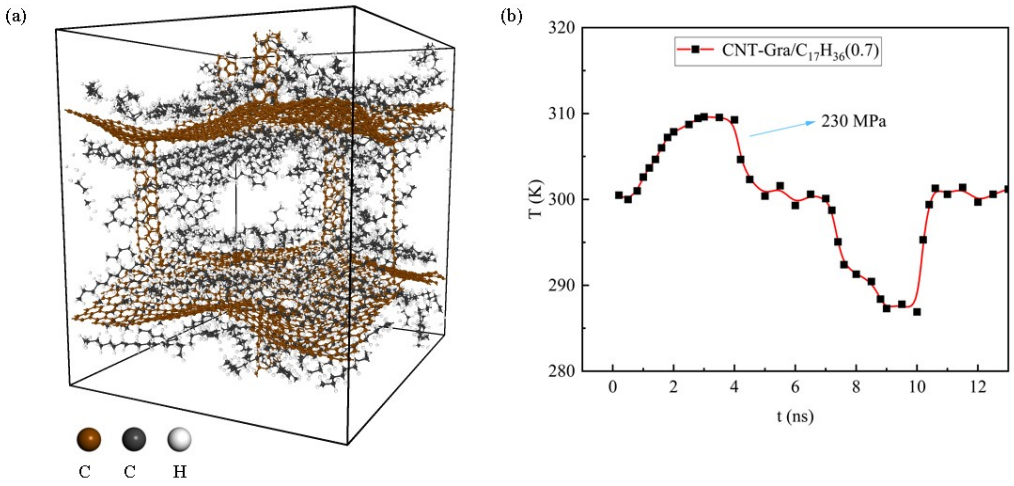

Figure SP7. (a) The structural state of CNT-Gra/$C_{17}H_{36}$ (0.7g/cm³) stretched by 20% along the Z-axis. (b) The relationship between the ΔT and time of CNT-Gra/$C_{17}H_{36}$ (0.7g/cm³) during adiabatic stretching along the Z-axis.

Fig. SP7(a) presents the state of a composite material CNT-Gra/$C_{17}H_{36}$ (0.7g/cm³) when stretched by 20% along the Z-direction. It is observed from the figure that,

although the deformation of the carbon CNT-Gra framework is not significant, the spacing between the $C_{17}H_{36}$ molecules has increased, manifesting as a dispersed state. Furthermore, through the analysis of Fig. SP7(b), we can determine that under a 20% stretching condition, the maximum adiabatic temperature change of this composite material is approximately 10 K. However, to achieve such a temperature change, an external stretching stress as high as 230 MPa is required. From the perspective of cooling effectiveness and energy efficiency, the performance of this stretching cooling method is not ideal, compared to the same level of compression cooling, it falls short in both efficiency and cooling effectiveness.

Tabel S1: Physical properties for leading elastocaloric materials shown in Figure 5. T_0 is the operating temperature. $|\Delta T_m|$ adiabatic temperature change from different experimental measurement methods, and the data obtained from direct measurements. $|\Delta\sigma|$ applied stress (pressure).

eC materials	T_0 (K)	$\lvert\Delta T_m\rvert$ (K)	Ref.
NiTi (wire)	300	25.5	[4]
NiTi (film)	260	16	[5]
$Cu_{83}Al_{14}Ni_3$	250	16	[6]
$Cu_{68.1}Zn_{15.8}Al_{16.1}$	300	16	[7, 8]
$Co_{40}Ni_{33.17}Al_{28.63}$	303	6	[9]
$Ni_{46}Mn_{38}Sb_{12}Co_4$	300	3	[10]
$(Ni_{50}Mn_{31.5}Ti_{18.5})_{99.8}B_{0.2}$	308	31.5	[11]
$Ni_{43}Mn_{40}Sn_{10}Cu_7$	320	38	[12]
$Fe_{49}Rh_{51}$	310	8.7	[13],[14]
$Ni_{31}Ti_{55}Cu_{12}Co_2$	280	10	[15]
$Ni_{50.5}Ti_{49.1}Fe_{0.4}$	200	17	[16]
$Ni_{48.4}Mn_{34.8}In_{16.8}$	300	4	[17]
$Ni_{50}Fe_{19}Ga_{27}Co_4$	348	10	[18]

Table S2: Physical properties for leading barocaloric materials shown in Figure 5. T_0 is the operating temperature. $|\Delta T_m|$ adiabatic temperature change from different experimental measurement methods, and the data obtained from direct measurements. $|\Delta\sigma|$ applied stress (pressure).

BC materials	T_0 (K)	$\lvert\Delta T_m\rvert$ (K)	Ref.
AgI	390	36	[19]
$(C_{10}H_{21}NH_3)_2MnC_{l4}$	314	31	[20]
1-Cl-ada	305	44	[21]
1-Br-ada	384	55	
C_{60}	257	9.7	[22]
NPG	313	22	[23]
NPA	235.7	16	[24]
PG	354	10	
PVDF-TrFE-CTFE	368	18.6	[25]
PDMS rubber	283	28.5	[26]

PDMS rubber	290	3.75	
ASR	250	21	[27]
$Ni_{49.26}Mn_{36.08}In_{14.66}$	290	4.5	[28]
$(MnNiSi)_{0.62}(FeCoGe)_{0.38}$	338	4.3	[29]
$BaTiO_3$	400	1	[30]
$(NH_4)_3MOO_3F_3$	297	15	[31]
[TPrA]Mn[dca]$_3$	330	5	[32]
$(NH_4)_2SO_4$	219	8	[33]
Rb_2KTiOF_5	215	18	[34, 35]
Mn_3GaN	285	1.3	[36]
n-alkanes	324	8	[37]

Table S3: The thermal conductivity [κ (W/ (m.K))] of various composite materials under different concentrations of normal alkanes [c (g/cm^3)] and in different directions (X, Y or Z).

κ (W/ (m.K))	X(Y)	Z
Amorphous-C_2H_6(0.5)	0.4	
Amorphous-C_2H_6(0.6)	0.43	
Amorphous-C_2H_6(0.7)	0.48	
Amorphous-C_9H_{20}(0.6)	0.39	
Amorphous-C_9H_{20}(0.7)	0.42	
Amorphous-$C_{17}H_{36}$(0.6)	0.28	
Amorphous-$C_{17}H_{36}$(0.7)	0.35	
Amorphous-$C_{17}H_{36}$(0.8)	0.4	
CNT-Gra/C_2H_6 (0.5)	15	3.7
CNT-Gra/C_2H_6 (0.6)	14.3	4.2
CNT-Gra/C_2H_6 (0.7)	13.6	4.8
CNT-Gra/C_5H_{12} (0.6)	14	3.9
CNT-Gra/C_9H_{20} (0.6)	13.5	3.68
CNT-Gra/$C_{17}H_{38}$ (0.6)	12.28	3.42
CNT-Gra/$C_{17}H_{38}$(0.7)	11.8	3.77
CNT-Gra/$C_{17}H_{38}$(0.8)	11	4.02

Detail of thermal conductivity:

To calculate the thermal conductivity of the composite materials, we employed the reverse non-equilibrium molecular dynamics (rNEMD) method. Reverse non-equilibrium molecular dynamics (rNEMD) based on the Muller-Plathe algorithm is a common method for studying thermal conductivity [42]. As shown in Fig. SP8, we set the middle of the simulation box as a heat source, and set the two ends of the simulation box as cold sources, and the simulation box has a periodic boundary. There are heat flux (dQ) and temperature gradient (dT/dZ), and the thermal conductivity can be calculated by the following formula [43]:

$$dQ = -\kappa \frac{dT}{dZ}, \tag{S5}$$

where dQ is the constant heat flux, κ is the thermal conductivity, and dT/dZ (dX, dY) is the temperature gradient along the Z (X, Y) direction.

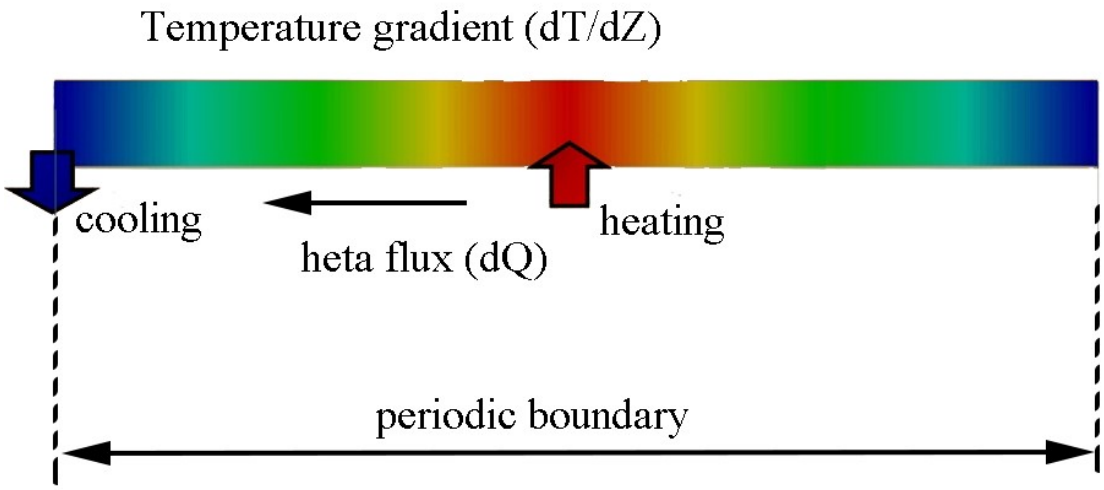

Figure SP8. Schematic diagram of reverse non-equilibrium molecular dynamics (rNEMD).

Our simulations were conducted for a total duration of 5 nanoseconds (ns); at this timescale, we observed stable behavior of heat flux and temperature gradients, ensuring the reliability of our results. To enhance statistical significance, we performed 5 independent simulations for each condition. Each simulation was initiated with different velocity distributions to avoid potential biases from the initial conditions.

Details of the PCFF potential

For our molecular dynamics (MD) simulations, we adopted the force field reported in the literature [2,3]. In LAMMPS software, the unit style we use is real[1].

The charge: q_{oh} = -0.57, q_{c4o} = 0.054, q_{c0} = 0.0, q_{c3} = -0.159, q_{ho} = 0.41, q_{hc} = 0.53.

The non-bond potential is given by:

$$E_{nonbond} = \sum_{non-bond} \{\varepsilon_{ij}[2(\frac{\sigma}{r_{ij}})^9 - 3(\frac{\sigma}{r_{ij}})^6] + \frac{q_i q_j}{4\pi\varepsilon_0 r_{ij}}\} \tag{S6}$$

q is the charge of atom, r_{ij} is the distance between two atoms within the truncation radius.

The bond potential is given by:

$$E_{bond} = \sum_{bond} [K_{b2}(b-b_0)^2 + K_{b3}(b-b_0)^3 + K_{b4}(b-b_0)^4] \tag{S7}$$

where b_0 is the equilibrium bond distance.

The angle potential is given by:

$$E_{angle} = \sum_{angle} [K_{a2}(\theta - \theta_0)^2 + K_{a3}(\theta - \theta_0)^3 + K_{a4}(\theta - \theta_0)^4] \quad \text{(S8)}$$

$$E_{bond/bond\ (bb)} = \sum_{bond/bond} K_{bb}(b - b_0)(b' - b_0') \quad \text{(S9)}$$

$$E_{bond/angle(ba)} = \sum_{bond/angle} K_{1ba}(b - b_1)(\theta - \theta_0) + K_{2ba}(b - b_2)(\theta - \theta_0) \quad \text{(S10)}$$

where E_{angle} is the angle term, $E_{bond/bond\ (bb)}$ is a bond-bond term, and $E_{bond/angle(ba)}$ is a bond-angle term. θ_0 is the equilibrium angle and b_1 and b_2 are the equilibrium bond lengths.

The dihedral potential is given by:

$$E_{torsion} = \sum_{torsion} [K_{t1}(1 - cos\emptyset) + K_{t2}(1 - cos2\emptyset) + K_{t3}(1 - cos3\emptyset)] \quad \text{(S11)}$$

$$E_{mbt} = (r_{jk} - r_2)[A_1\cos(\phi) + A_2\cos(2\phi) + A_3\cos(3\phi)] \quad \text{(S12)}$$

$$E_{ebt} = (r_{ij} - r_1)[B_1\cos(\phi) + B_2\cos(2\phi) + B_3\cos(3\phi)] + (r_{kl} - r_3)[C_1\cos(\phi) + \quad \text{(S13)}$$

$$E_{at} = (\theta_{ijk} - \theta_1)[D_1\cos(\phi) + D_2\cos(2\phi) + D_3\cos(3\phi)] + (\theta_{jkl} - \quad [E_1\cos(\phi) + E_2\cos(2\phi) + E_3\cos(3\phi)] \quad \text{(S14)}$$

$$E_{aat} = M(\theta_{ijk} - \theta_1)(\theta_{jkl} - \theta_2)\cos(\phi) \quad \text{(S15)}$$

$$E_{bb13} = N(r_{ij} - r_1)(r_{kl} - r_3) \quad \text{(S16)}$$

where $E_{torsion}$ is the dihedral term, E_{mbt} is a middle-bond-torsion term, E_{ebt} is an end-bond-torsion term, E_{at} is an angle-torsion term, E_{aat} is an angle-angle-torsion term, and

E_{bb13} is a bond-bond-13 term. θ_1 and θ_2 are equilibrium angles and r_1, r_2 and r_3 are equilibrium bond lengths.

The dihedral potential is given by:

$$E_{aa} = M_1(\theta_{ijk} - \theta_1)(\theta_{kjl} - \theta_3) + M_2(\theta_{ijk} - \theta_1)(\theta_{ijl} - \theta_2) + M_3(\theta_{ijl} - (\theta_{kjl} - \theta_3) \quad \text{(S17)}$$

where E_{aa} is an angle-angle term. θ_{ijl} is the angle formed by atoms i, j, and l with j in the middle. θ_1, θ_2 and θ_3 are the equilibrium positions of those angles. Atom j (the second atom in the quadruplet) is the atom of symmetry in the theta angles, since it is always the center atom.

The parameters corresponding to all formulas are implemented into **MedeA**[37], the atomic simulation program used in the present work.

Table S4. The parameters of non-bond potential.

Non-bond	ε	σ
c0	0.007	3.75
c40	0.0748	3.87
c=2	0.081	3.91
cp	0.0668	3.9147
hc	0.023	2.878
oh	0.008	1.087
ho	0.096	3.58

Table S5. The parameters of bond potential.

Bond	b_0	K_{b2}	K_{b3}	K_{b4}
c40-hc	1.101	345	-691.89	844.6
c40-oh	1.42	400.4	-835.2	1313
c0-c40	1.53	299.67	-501.77	679.81
ho-oh	1.42	400.4	-835.2	1313
cp-cp	1.417	470.84	-627.62	1327.6
c=2-cp	1.5	322.8	0	0
c0-cp	1.501	321.9	521.82	572.16

Table S6. The parameters of angle potential.

Angle	θ_0	K_{a2}	K_{a3}	K_{a4}
hc-c40-hc	107.66	39.641	-12.921	-2.4318
hc-c40-oh	108.73	58.545	-10.809	-12.401
c0-c40-hc	110.77	41.453	-10.604	-5.129
c0-c40-oh	111.27	54.538	-8.3642	-13.084
c40-oh-ho	105.8	52.706	-12.109	-9.8681
c40-c0-c40	112.67	39.516	-7.443	-9.5583
cp-cp-cp	118.9	61.023	-34.993	0
-c=2-	120	60	0	0
-cp-	120	65	0	0

Table S7. The parameters of angle potential (**bb**).

Angle	K_{bb}	b_0	b'_0
hc-c40-hc	5.3316	1.101	1.101
hc-c40-oh	23.198	1.101	1.42
c0-c40-hc	3.3872	1.53	1.01
c0-c40-oh	11.432	1.53	1.42
c40-oh-ho	-9.6879	1.42	0.965
c40-c0-c40	0	1.53	1.53
cp-cp-cp	68.286	1.417	1.417
-c=2-	0	1.5	1.5
-cp-	0	1.5	1.5

Table S8. The parameters of angle potential (**ba**).

Angle	K_{1ba}	b_1	K_{2ba}	b_2
hc-c40-hc	18.103	18.103	1.101	1.101
hc-c40-oh	4.6198	55.327	1.101	1.42
c0-c40-hc	20.754	11.421	1.53	1.101
c0-c40-oh	2.6868	20.403	153	1.42
c40-oh-ho	28.58	18.928	1.42	0.965
c40-c0-c40	8.016	8.016	1.53	1.53
cp-cp-cp	28.871	28.871	1.417	1.417
-c=2-	0	0	1.5	1.5
-cp-	0	0	1.5	1.417

References

[1] A. P. Thompson et al., Comput. Phys. Commun. **271**, 108171 (2022).

[2] H. Sun, J. Phys. Chem. B **1998**, 102, 7338-7364.

[3] H. Sun, Z. Jin, C. Yang, R.L.C. Akkermans, S.H. Robertson, N.A. Spenley, S. Miller, and S.M. Todd, J Mol Model **22**(2), 47 (2016).

[4] J. Cui, Y. Wu, J. Muehlbauer, Y. Hwang, R. Radermacher, S. Fackler, M. Wuttig, I. Takeuchi, *Appl. Phys. Lett.* **2012**, 101, 073904.

[5] H. Ossmer, F. Lambrecht, M. Gültig, C. Chluba, E. Quandt, M. Kohl, *Acta Mater.* **2014**, 81, 9.

[6] C. Rodriguez, L. Brown, *Metall. Mater. Trans. A* **1980**, 11, 147.

[7] E. Bonnot, R. Romero, L. Mañosa, E. Vives, A. Planes, *Phys. Rev. Lett.* **2008**, 100, 125901.

[8] E. Vives, S. Burrows, R. S. Edwards, S. Dixon, L. Mañosa, A. Planes, R. Romero, *Appl. Phys. Lett.* **2011**, 98, 011902.

[9] G. J. Pataky, E. Ertekin, H. Sehitoglu, *Acta Mater.* **2015**, 96, 420.

[10] R. Millán-Solsona, E. Stern-Taulats, E. Vives, A. Planes, J. Sharma, A. K. Nayak, K. Suresh, L. Mañosa, *Appl. Phys. Lett.* **2014**, 105, 241901.

[11] D. Cong, W. Xiong, A. Planes, Y. Ren, L. Mañosa, P. Cao, Z. Nie, X. Sun, Z. Yang, X. Hong, *Phys. Rev. Lett.* **2019**, 122, 255703.

[12] P. O. Castillo-Villa, L. Mañosa, A. Planes, D. E. Soto-Parra, J. L. Sánchez-Llamazares, H. Flores-Zúñiga, C. Frontera, *J. Appl. Phys.* **2013**, 113, 053506.

[13] M. Annaorazov, S. Nikitin, A. Tyurin, K. Asatryan, A. K. Dovletov, *J. Appl. Phys.* **1996**, 79, 1689.

[14] S. Nikitin, G. Myalikgulyev, M. Annaorazov, A. Tyurin, R. Myndyev, S. Akopyan, *Phys. Lett. A* **1992**, 171, 234.

[15] C. Chluba, H. Ossmer, C. Zamponi, M. Kohl, E. Quandt, *Shap. Mem. Superelasticity* **2016**, 2, 95.

[16] H. Ossmer, C. Chluba, M. Gueltig, E. Quandt, M. Kohl, *Shap. Mem. Superel.* **2015**, 1, 142.

[17] Y. Huang, Q. Hu, N. Bruno, J.-H. Chen, I. Karaman, J. H. Ross Jr, J. Li, *Scripta Mater.* **2015**, 105, 42.

[18] F. Xiao, M. Jin, J. Liu, X. Jin, *Acta Mater.* **2015**, 96, 292.

[19] A. Aznar, P. Lloveras, M. Romanini, M. Barrio, J.-L. Tamarit, C. Cazorla, D. Errandonea, N. D. Mathur, A. Planes, X. Moya, *Nat. Commun.* **2017**, 8, 1.

[20] J. Li, M. Barrio, D. J. Dunstan, R. Dixey, X. Lou, J. L. Tamarit, A. E. Phillips, P. Lloveras, *Adv. Funct. Mater.* **2021**, 31, 2105154.

[21] A. Aznar, P. Negrier, A. Planes, L. Mañosa, E. Stern-Taulats, X. Moya, M. Barrio, J.-L. Tamarit, P. Lloveras, *Appl. Mater. Today* 2021, 23, 101023.

[22] J. Li, D. Dunstan, X. Lou, A. Planes, L. Mañosa, M. Barrio, J.-L. Tamarit, P. Lloveras, *J. Mater. Chem.* A 2020, 8, 20354.

[23] P. Lloveras, A. Aznar, M. Barrio, Ph. Negrier, C. Popescu, A. Planes, L. Mañosa, E. Stern-

Taulats, A. Avramenko, N.D. Mathur, X. Moya, and J.-Ll. Tamarit, Nat Commun 10(1), 1803 (2019).

[24] A. Aznar, P. Lloveras, M. Barrio, P. Negrier, A. Planes, L. Mañosa, N. D. Mathur, X. Moya, J.-L. Tamarit, *J. Mater. Chem. A* **2020**, 8, 639.

[25] S. Patel, A. Chauhan, R. Vaish, P. Thomas, *Appl. Phys. Lett.* **2016**, 108, 072903.

[26] A. Carvalho, W. Imamura, E. Usuda, N. Bom, *Eur. Polym. J.* **2018**, 99, 212.

[27] W. Imamura, É. O. Usuda, L. S. Paixão, N. M. Bom, A. M. Gomes, A. M. G. Carvalho, *Chinese J. Polym. Sci.* **2020**, 38, 999.

[28] L. Mañosa, D. González-Alonso, A. Planes, E. Bonnot, M. Barrio, J.-L. Tamarit, S. Aksoy, M. Acet, *Nat. Mater.* **2010**, 9, 478.

[29] T. Samanta, P. Lloveras, A. Us Saleheen, D. L. Lepkowski, E. Kramer, I. Dubenko, P. W. Adams, D. P. Young, M. Barrio, J. L. Tamarit, *Appl. Phys. Lett.* **2018**, 112, 021907.

[30] E. Stern-Taulats, P. Lloveras, M. Barrio, E. Defay, M. Egilmez, A. Planes, J.-L. Tamarit, L. Mañosa, N. Mathur, X. Moya, *APL Mater.* **2016**, 4, 091102.

[31] I. Flerov, M. Gorev, A. Tressaud, N. Laptash, *Crystallogr. Rep.* **2011**, 56, 9.

[32] J. M. Bermúdez-García, M. Sánchez-Andújar, S. Castro-García, J. López-Beceiro, R. Artiaga, M. A. Señarís-Rodríguez, *Nat. Commun.* **2017**, 8, 1.

[33] P. Lloveras, E. Stern-Taulats, M. Barrio, J.-L. Tamarit, S. Crossley, W. Li, V. Pomjakushin, A. Planes, L. Mañosa, N. Mathur, *Nat. Commun.* **2015**, 6, 1.

[34] M. Gorev, E. Bogdanov, I. Flerov, V. Voronov, N. Laptash, *Ferroelectrics* **2010**, 397, 76.

[35] V. Fokina, I. Flerov, M. Molokeev, E. Pogorel'tsev, E. Bogdanov, A. Krylov, A. Bovina, V. Voronov, N. Laptash, *Phys. Solid State.* **2008**, 50, 2175.

[36] D. Matsunami, A. Fujita, K. Takenaka, M. Kano, *Nat. Mater.* **2015**, 14, 73.

[37] J. Lin, P. Tong, K. Zhang, K. Tao, W. Lu, X. Wang, X. Zhang, W. Song, Y. Sun, *Nat. Commun.* **2022**, 13, 1.

[38] https://www.materialsdesign.com

[39] Zhang, T., Li, X., & Gao, H. (2015). Fracture of graphene: a review. International Journal of Fracture, 196, 1-31.

[40] S. Smidstrup, T. Markussen, P. Vancraeyveld, J. Wellendorff, J. Schneider, T. Gunst, B. Verstichel, D. Stradi, P.A. Khomyakov, U.G. Vej-Hansen, M.-E. Lee, S.T. Chill, F. Rasmussen, G. Penazzi, F. Corsetti, A. Ojanperä, K. Jensen, M.L.N. Palsgaard, U. Martinez, A. Blom, M. Brandbyge, and K. Stokbro, J. Phys.: Condens. Matter 32(1), 015901 (2020).

[41] Grimme, S.; Antony, J.; Ehrlich, S.; Krieg, H. J. Chem. Phys. 2010, 132, 154104

[42] M. Zhang, E. Lussetti, L.E.S. De Souza, and F. Müller-Plathe,J. Phys. Chem. B 109(31), 15060–15067 (2005).

[43] F. Müller-Plathe, The Journal of Chemical Physics 106(14), 6082–6085 (1997).

[44] C. Cazorla, "Novel mechanocaloric materials for solid-state cooling applications," Applied Physics Reviews **6**(4), 041316 (2019)

[45] F. Liu, N. Hu, and W. F. Yuan et al, "The interfacial mechanical properties of functionalized graphene–polymer nanocomposites**" RSC Adv., 6, 66658, 2016,**